Correlation-driven Topological Phases in Magic Angle Twisted Bilayer Graphene

Youngjoon Choi[1,2,3*], Hyunjin Kim[1,2,3*], Yang Peng[4,3], Alex Thomson[2,3,5], Cyprian Lewandowski[2,3,5], Robert Polski[1,2], Yiran Zhang[1,2,3], Harpreet Singh Arora[1,2], Kenji Watanabe[6], Takashi Taniguchi[6], Jason Alicea[2,3,5], Stevan Nadj-Perge[1,2†]

[1]*T. J. Watson Laboratory of Applied Physics, California Institute of Technology, 1200 East California Boulevard, Pasadena, California 91125, USA*
[2]*Institute for Quantum Information and Matter, California Institute of Technology, Pasadena, California 91125, USA*
[3]*Department of Physics, California Institute of Technology, Pasadena, California 91125, USA*
[4]*Department of Physics and Astronomy, California State University, Northridge, California 91330, USA*
[5]*Walter Burke Institute for Theoretical Physics, California Institute of Technology, Pasadena, California 91125, USA*
[6]*National Institute for Materials Science, Namiki 1-1, Tsukuba, Ibaraki 305 0044, Japan*
**These authors contributed equally to this work*
[†]*Correspondence: s.nadj-perge@caltech.edu*

Magic-angle twisted bilayer graphene (MATBG) exhibits a range of correlated phenomena that originate from strong electron-electron interactions. These interactions make the Fermi surface highly susceptible to reconstruction when $\pm 1, \pm 2, \pm 3$ electrons occupy each moiré unit cell and lead to the formation of various correlated phases[1–4]. While some phases have been shown to carry a non-zero Chern number[5,6], the local microscopic properties and topological character of many other phases remain elusive. Here we introduce a set of novel techniques hinging on scanning tunneling microscopy (STM) to map out topological phases in MATBG that emerge in finite magnetic field. By following the evolution of the local density of states (LDOS) at the Fermi level with electrostatic doping and magnetic field, we visualize a local Landau fan diagram that enables us to directly assign Chern numbers to all observed phases. We uncover the existence of six topological phases emanating from integer fillings in finite fields and whose origin relates to a cascade of symmetry-breaking transitions driven by correlations[7,8]. These topological phases can form only in a small range of twist angles around the magic-angle value which further differentiates them from the Landau levels observed near charge neutrality. Moreover, we observe that even the charge-neutrality Landau spectrum taken at low fields is considerably modified by interactions and exhibits prominent electron-hole asymmetry and features an unexpectedly large splitting between zero Landau levels ($\sim 3-5$ meV). Our results show how strong electronic interactions impact the MATBG band structure and lead to correlation-enabled topological phases.

MATBG features a triangular moiré lattice with a period $\mathrm{L_m} = a/(2\sin(\theta/2)) \approx 13$ nm set by the twist angle $\theta \approx 1.1^\circ$ and the graphene lattice constant $a = 0.246$ nm[9,10]. This additional spa-

tial periodicity gives rise to an effective mini-Brillouin zone, which due to its small-size is expected to give rise to topological Chern insulating phases at realistic magnetic fields[11–14] characteristic of a Hofstadter's spectrum[15,16]. Yet the impact of strong correlations on Hofstadter physics and resulting topological phases in MATBG is still underexplored. We study MATBG placed on a tungsten diselenide (WSe_2) monolayer, thick hBN dielectric layer and graphite gate; see Fig. fig: fig1a as well as Extended Data Fig. 1 and Methods, section 1. We use monolayer WSe_2 as a MATBG immediate substrate since previous work[17] suggests that WSe_2 improves the sample quality and does not change the magic-angle condition. In STM, twist angle can be determined by measuring the distance between neighbouring AA moiré sites in the topographic data (Fig. 1b)[18–20]. Measured quantity, tunneling conductance ($\mathrm{dI/dV}$), corresponding to the local density of states (LDOS), as a function of sample bias ($\mathrm{V_{Bias}}$) and a gate voltage ($\mathrm{V_{Gate}}$) that tunes electrostatic doping, shows the evolution of the two LDOS peaks originating from the Van Hove singularities (VHS) of the flat bands (Fig. 1c). At $\mathrm{V_{Gate}} > +5$V, both peaks are below the Fermi energy ($\mathrm{E_F}$, $\mathrm{V_{Bias}} = 0$ mV), indicating completely filled flat bands. As $\mathrm{V_{Gate}}$ is reduced, the first VHS corresponding to the conduction flat band crosses $\mathrm{E_F}$ several times, resetting its position around gate voltages corresponding to occupations of $\nu = 3, 2, \text{ and } 1$ electrons per moiré unit cell until the $\nu = 0$ charge neutrality point (CNP) is reached—at which the splitting between VHS is maximized[19–22] (See Methods, section 4, for assigning of filling factor ν to $\mathrm{V_{Gate}}$). A similar cascade was previously observed in MATBG placed directly on hBN[8]; our observations thus demonstrate that the added WSe_2 does not significantly alter the spectrum or the cascade mechanics.

Landau levels in MATBG

In a perpendicular magnetic field, the overall spectrum changes as Landau levels (LLs) develop in the flat bands around the CNP, and the onsets of the cascade transitions shift accordingly (see black arrows in Fig. 1d,e). These onsets are accompanied by a low LDOS at $\mathrm{E_F}$ and nearly horizontal resonance peaks, indicating the presence of gapped states[23]. Focusing first on identifying LLs near the CNP, a linecut at $\mathrm{B} = 8$ T shows four well-resolved peaks (Fig. 1f). The phenomenological ten-band model[24] with parameters chosen to semi-quantitatively match the data (Fig. 1g) suggests that the inner peaks are zero LLs (zLLs) originating from MATBG Dirac points, while the outer peaks (that include the VHS) form from the LLs that descend from less-dispersive parts of the band structure and can not be individually resolved. Importantly, both zLLs and the broad-feature that includes VHS are expected to be four-fold spin-valley degenerate and carry non-zero Chern number ($+1$ and -1 respectively per spin and valley flavor, see also Methods, section 8a). For simplicity, we will refer to the $C = -1$ broad-feature (that consist of non-resolved LLs and includes VHS) as a simply VHS. In this notation, the total Chern number of zLL (VHS) is $C = +4$ ($C = -4$). The four-fold degeneracy of zLLs is further corroborated by observing the splitting into four distinct branches, when each of the zLLs crosses the Fermi energy (Extended Data Fig. 4). The Chern number assignment takes into account splitting of Dirac cones in energy that is experimentally observed via two inner peaks instead of one and accounts for the reduction of an eight- to four-fold degeneracy observed in previous transport MATBG experiments (see Methods, sections 8a and 7b).

With this interpretation in mind, and as discussed in the remainder of the paper, we attribute the shifting of the zero-field cascades (black arrows in Fig. 1d and Fig. 1e; see also Methods, section 6 and Extended Data Fig. 3) and the accompanying gaps to the formation of Chern insulating phases enabled by correlations.

LDOS Landau fan diagram

The spectrum of MATBG in magnetic fields has so far been studied using transport measurements that provide information about electronic structure close to $\mathrm{E_F}$[1,3,4,25]. We relate these experiments to our STM findings by utilizing a novel approach that enables measuring a full Landau fan diagram via LDOS. This LDOS Landau fan is acquired by taking the tunneling conductance without feedback and keeping $\mathrm{V_{Bias}} = 0$ mV, such that the STM probes MATBG at $\mathrm{E_F}$ as electron density ($\mathrm{V_{Gate}}$)[20] and magnetic field are varied. The resulting signal, reflecting LDOS at $\mathrm{E_F}$, is thus suppressed in certain regions of carrier densities where gaps develop (Fig. 2a and b).

Our LDOS Landau fan (Fig. 2c), taken at one specific AB point, reproduces many of the features established in previous MATBG magneto-transport measurements[1,3,4,17] despite the fact that it records a fundamentally different quantity—LDOS instead of transport resistance. The approach also allows verifying whether the twist angle values extracted from the Landau fan match the ones seen in topography (agreement is within 0.01°). Importantly, in addition to LLs, we also observe strong LDOS suppressions that abruptly appear in finite fields ($\mathrm{B} > 3$ T for $\nu > 0$ and $\mathrm{B} > 6$ T for $\nu < 0$; red dashed lines in Fig. 2c), indicating the formation of insulating phases emanating from ν = ± 1, ± 2, and $+3$ [26–28]. The corresponding Chern numbers, $C = \pm 3$, ± 2, and $+1$, respectively, can directly be assigned from the observed slopes of the gap positions as a function of ν and the Diophantine equation[29], $\nu(\mathrm{B}) = C \times \mathrm{A_m} \times \mathrm{B}/\phi_0 + \nu(\mathrm{B} = 0)$ (see Extended Data Fig. 6 for data showing the $C = -1$ state). Here $\mathrm{A_m} = \sqrt{3}\mathrm{L_m}^2/2$ is the moiré unit cell area, ϕ_0 is the flux quantum, and $\nu(\mathrm{B} = 0)$ denotes the filling ($\pm 1, \pm 2, +3$) from which the phases emanate.

Correlated Chern insulating phases

To better understand how Chern phases develop, we perform spectroscopic measurements for fixed magnetic field (Fig. 2d). Focusing on the conduction flat band, as the gate voltage increases from $\mathrm{V_{Gate}} \approx 2$ V, the four-fold degenerate VHS approaches the Fermi level. Just before crossing ($\mathrm{V_{Gate}} \approx 3$ V), a series of small gaps open up, accompanied by a set of nearly horizontal resonance peaks. These resonances are attributed to quantum dot formation around the tip due to the emergence of a fully gapped insulating state in its vicinity (see also Methods, section 5). As $\mathrm{V_{Gate}}$ further increases, part of the VHS-LDOS feature is abruptly pushed up in energy (seen at higher $\mathrm{V_{Bias}}$ in Fig. 2d), reducing its spectral weight. Similar transitions are observed also near $\mathrm{V_{Gate}} \approx 4$ V and $\mathrm{V_{Gate}} \approx 5.1$ V with the spectral weight reducing after each transition. This tran-

sition sequence is analogous to the $\mathrm{B} = 0$ T cascade, though with the finite-field, onsets shifted to new $\mathrm{V_{Gate}}$ positions that trail the location of nearby Chern insulating phases (see also the additional discussion in Methods, section 6 and Extended Data Fig. 3).

These observations can be explained within the Hofstadter picture (Fig. 1f,g), where each zLL carries total Chern number $C = +4$ and the VHS, carries $C = -4$. Here the factors of four reflecting spin-valley flavor degeneracy. When the conduction band's VHS is empty, the Chern number of the occupied bands is $C = -4 + 4 \times 2 = +4$ (here -4 comes from the valence band VHS, while $+4 \times 2$ comes from zLLs). Consequently, the gap between the zLL and the bottom of the VHS follows the corresponding $C = +4$ slope in the LDOS Landau emanating from CNP (marked with the gray line labeled $+4$ in Fig. 2c). As charge density increases, all four spin-valley flavors in the conduction band are populated equally, until the VHS reaches $\mathrm{E_F}$ and interactions underlying the cascade[7] shift all carriers to one flavor VHS while the other three are pushed to higher energies (Fig. 2e). Since the added single-flavor VHS carries $C = -1$, the total Chern number is now $C = +3$, and the next corresponding gap in the LDOS Landau fan follows an accordingly reduced slope. This sequence repeats, creating a cascade.

Angle dependence

To verify the role of correlations on the Chern insulating phases, we extend the technique introduced in Fig. 2a-c to visualize the evolution of these phases with twist angle. For this purpose, we focus on an area where the angle slowly changes over hundreds of nanometers (many moiré periods), so that twist angle is locally well-defined and the strain is low ($<0.3\%$) (Fig. 3a). By measuring the LDOS at $\mathrm{E_F}$ vs. $\mathrm{V_{Gate}}$ and spatial position, we image the development of the Chern phases and the zLLs (Fig. 3b). While LL gaps around the CNP form at filling factor $\nu_{LL} = \pm 4, \pm 2, 0$ at fixed $\mathrm{V_{Gate}}$ independent of the twist angle, the Chern insulating phases move away from the CNP for larger angles as expected from the change of the moiré unit cell size. The Chern insulating phases are also only observed in a certain narrow range around the magic angle (Fig. 3b), highlighting the importance of correlations for their formation. For example, the $C = -3$ state emanating from $\nu = -1$ appears only for $1.02° < \theta < 1.14°$ at $\mathrm{B} = 7$ T while the $C = -2$ state is stable for a slightly larger range. Moreover, at lower fields, the angle range where the Chern phases are visible also diminishes (Fig. 3c-e). The phase diagram (Fig. 3f) thus depends sensitively on both magnetic field and twist angle.

The observed evolution of Chern insulators with twist angle reflects a competition between Coulomb interactions and kinetic energy, similarly to the cascade at $\mathrm{B} = 0$ T. Here the electron-electron interaction scale is approximately set by $U \approx e^2/4\pi\epsilon\mathrm{L_m}$ (e and ϵ respectively denote the electron charge and dielectric constant) and increases for larger twist angle. The typical kinetic energy scale, taken to be the bandwidth W of the $C = -1$ single flavor VHS, instead exhibits non-monotonic twist-angle dependence, and is minimal at the magic angle and further narrows with increasing magnetic field. We thus expect Chern insulating phases to occur close to the magic

angle, with larger fields required for their onset away from the magic angle (Fig. 3f). Estimates of U/W as a function of B based on a continuum model support this reasoning (see Methods, section 8). Further, we note a general electron-hole asymmetry of the angle range where Chern phases are observed (Fig. 3b): the $C = -2$ phase emanating from $\nu = -2$ on the hole side is seen for $1.19° > \theta > 1.01°$, while the $C = 2$ state on the electron side is observed for $1.15° > \theta$ down to $0.99°$. This observation indicates that the 'magic angle' condition where correlations are strongest differs between the conduction and valence flat bands and highlights the sensitivity of MATBG physics to tiny twist-angle changes.

Spectroscopy of Landau levels near CNP

Now we explore low-magnetic-field LLs observed near the CNP, which are directly relevant for the MATBG band structure. Many MATBG properties remain poorly understood—e.g., the appearance of four-fold degenerate LLs around charge neutrality[1] instead of eight-fold as expected from the eight degenerate Dirac cones of the two stacked monolayers, and the measured flat-band bandwidth ($\sim$ 40 meV)[19–22] that far exceeds theoretical predictions[10]. These discrepancies are largely due to difficulties in performing band-structure calculations that incorporate electronic correlations[30–32], strain[33] and atomic reconstruction[34]. Several mechanisms were proposed to explain the four-fold degenerate LLs formed at charge neutrality[33,35,36], although no general consensus has emerged. Figure 4a-f shows the evolution of CNP LLs for 0.5 T$< \mathrm{B} < 4$ T. The four-fold LL degeneracy, revealed in Fig. 2c, is seen here through the equal separation between LLs in $\mathrm{V_{Gate}}$ as they cross $\mathrm{E_F}$ (see ν_{LL} marked in Fig. 4f and the compare color coding from the diagram in Fig. 2c). Here, we focus on the relative energy separation between LLs taken at fixed $\mathrm{V_{Gate}}$ while varying B (Fig. 4g-i). Since the energy separation between LLs can be affected by exchange interactions when LLs cross the Fermi energy, we choose $\mathrm{V_{Gate}}$ values to avoid such interaction-altered regions and compile the single-particle energy spectrum in Fig. 4j. We note that, although fine features of the LL spectrum may vary with spatial location, the energy separations remain similar.

The observed LL spectrum is consistent with a scenario wherein the two moiré Brillouin zone Dirac cones are shifted in energy, either by strain (0.3% in this area)[33,36] or layer polarization due to a displacement field[37] (see also Methods, section 10). In this scenario, $0+$ and $0-$ (Fig. 4j) originate from the two Dirac points and the spectrum can be compared to the Dirac-like dispersion $E_n = sgn(n)v_D\sqrt{2e\hbar|n|\mathrm{B}}$ with $sgn(n) = n/|n|$. The observed LL separations (e.g., 8 meV for $0-$ to $1-$ and 5 meV for $1-$ to $2-$ at $\mathrm{B} = 2$ T) yield a Dirac velocity $v_D \approx 1.5 - 2 \times 10^5$ m/s than exceeds continuum-model predictions by an order of magnitude, highlighting possible interaction-induced modification of MATBG bands near the CNP. Electron-hole asymmetry is also present, as the energy differences between the first few LLs on the hole side are larger than their electron-side counterparts. Moreover, upon doping, LLs move together toward the VHS while the separation between them is hardly affected (Fig. 4a,c,e). This finding signals that dispersive pockets within the flat bands do not change significantly as flatter parts of the bands deform[30,31]. Together these observations place strict restrictions on the MATBG electronic bands and provide guidance for

further theoretical modeling. Looking ahead, we anticipate that the novel STM spectroscopic techniques developed here will enable the exploration of other exotic phases in MATBG and related moiré systems.

Note: In the course of preparation of this manuscript we became aware of the related work[38].

References:

1. Cao, Y. *et al.* Correlated insulator behaviour at half-filling in magic-angle graphene superlattices. *Nature* **556**, 80–84 (2018).

2. Cao, Y. *et al.* Unconventional superconductivity in magic-angle graphene superlattices. *Nature* **556**, 43–50 (2018).

3. Yankowitz, M. *et al.* Tuning superconductivity in twisted bilayer graphene. *Science* **363**, 1059–1064 (2019).

4. Lu, X. *et al.* Superconductors, orbital magnets and correlated states in magic-angle bilayer graphene. *Nature* **574**, 653–657 (2019).

5. Sharpe, A. L. *et al.* Emergent ferromagnetism near three-quarters filling in twisted bilayer graphene. *Science* **365**, 605–608 (2019).

6. Serlin, M. *et al.* Intrinsic quantized anomalous Hall effect in a moiré heterostructure. *Science* (2019).

7. Zondiner, U. *et al.* Cascade of phase transitions and Dirac revivals in magic-angle graphene. *Nature* **582**, 203–208 (2020). 1912.06150.

8. Wong, D. *et al.* Cascade of transitions between the correlated electronic states of magic-angle twisted bilayer graphene. *arXiv:1912.06145 [cond-mat]* (2019). 1912.06145.

9. Lopes dos Santos, J. M. B., Peres, N. M. R. & Castro Neto, A. H. Graphene Bilayer with a Twist: Electronic Structure. *Physical Review Letters* **99**, 256802 (2007).

10. Bistritzer, R. & MacDonald, A. H. Moiré bands in twisted double-layer graphene. *Proceedings of the National Academy of Sciences* **108**, 12233–12237 (2011).

11. Hunt, B. *et al.* Massive Dirac Fermions and Hofstadter Butterfly in a van der Waals Heterostructure. *Science* **340**, 1427–1430 (2013).

12. Ponomarenko, L. A. *et al.* Cloning of Dirac fermions in graphene superlattices. *Nature* **497**, 594–597 (2013).

13. Dean, C. R. *et al.* Hofstadter's butterfly and the fractal quantum Hall effect in moiré superlattices. *Nature* **497**, 598–602 (2013).

14. Wang, L. *et al.* Evidence for a fractional fractal quantum Hall effect in graphene superlattices. *Science* **350**, 1231–1234 (2015).

15. Hofstadter, D. R. Energy levels and wave functions of Bloch electrons in rational and irrational magnetic fields. *Physical Review B* **14**, 2239–2249 (1976).

16. Bistritzer, R. & MacDonald, A. H. Moir\'e butterflies in twisted bilayer graphene. *Physical Review B* **84**, 035440 (2011).

17. Arora, H. S. *et al.* Superconductivity in metallic twisted bilayer graphene stabilized by WSe 2. *Nature* **583**, 379–384 (2020).

18. Brihuega, I. *et al.* Unraveling the Intrinsic and Robust Nature of van Hove Singularities in Twisted Bilayer Graphene by Scanning Tunneling Microscopy and Theoretical Analysis. *Physical Review Letters* **109**, 196802 (2012).

19. Kerelsky, A. *et al.* Maximized electron interactions at the magic angle in twisted bilayer graphene. *Nature* **572**, 95–100 (2019).

20. Choi, Y. *et al.* Electronic correlations in twisted bilayer graphene near the magic angle. *Nature Physics* **15**, 1174–1180 (2019).

21. Xie, Y. *et al.* Spectroscopic signatures of many-body correlations in magic-angle twisted bilayer graphene. *Nature* **572**, 101–105 (2019).

22. Jiang, Y. *et al.* Charge order and broken rotational symmetry in magic-angle twisted bilayer graphene. *Nature* **573**, 91–95 (2019).

23. Jung, S. *et al.* Evolution of microscopic localization in graphene in a magnetic field from scattering resonances to quantum dots. *Nature Physics* **7**, 245–251 (2011).

24. Po, H. C., Zou, L., Senthil, T. & Vishwanath, A. Faithful tight-binding models and fragile topology of magic-angle bilayer graphene. *Physical Review B* **99**, 195455 (2019).

25. Uri, A. *et al.* Mapping the twist-angle disorder and Landau levels in magic-angle graphene. *Nature* **581**, 47–52 (2020).

26. Saito, Y. *et al.* Hofstadter subband ferromagnetism and symmetry broken Chern insulators in twisted bilayer graphene. *arXiv:2007.06115 [cond-mat]* (2020). 2007.06115.

27. Wu, S., Zhang, Z., Watanabe, K., Taniguchi, T. & Andrei, E. Y. Chern Insulators and Topological Flat-bands in Magic-angle Twisted Bilayer Graphene. *arXiv:2007.03735 [cond-mat]* (2020). 2007.03735.

28. Das, I. *et al.* Symmetry broken Chern insulators and magic series of Rashba-like Landau level crossings in magic angle bilayer graphene. *arXiv:2007.13390 [cond-mat]* (2020). 2007.13390.

29. Wannier, G. H. A Result Not Dependent on Rationality for Bloch Electrons in a Magnetic Field. *physica status solidi (b)* **88**, 757–765 (1978).

30. Guinea, F. & Walet, N. R. Electrostatic effects, band distortions, and superconductivity in twisted graphene bilayers. *Proceedings of the National Academy of Sciences* **115**, 13174–13179 (2018).

31. Goodwin, Z. A. H., Vitale, V., Liang, X., Mostofi, A. A. & Lischner, J. Hartree theory calculations of quasiparticle properties in twisted bilayer graphene. *arXiv:2004.14784 [cond-mat]* (2020). 2004.14784.

32. Xie, M. & MacDonald, A. H. Nature of the Correlated Insulator States in Twisted Bilayer Graphene. *Physical Review Letters* **124**, 097601 (2020).

33. Bi, Z., Yuan, N. F. Q. & Fu, L. Designing flat bands by strain. *Physical Review B* **100**, 035448 (2019).

34. Nam, N. N. T. & Koshino, M. Lattice relaxation and energy band modulation in twisted bilayer graphene. *Physical Review B* **96**, 075311 (2017).

35. Hejazi, K., Liu, C. & Balents, L. Landau levels in twisted bilayer graphene and semiclassical orbits. *Physical Review B* **100**, 035115 (2019).

36. Zhang, Y.-H., Po, H. C. & Senthil, T. Landau level degeneracy in twisted bilayer graphene: Role of symmetry breaking. *Physical Review B* **100**, 125104 (2019).

37. Carr, S., Fang, S., Po, H. C., Vishwanath, A. & Kaxiras, E. Derivation of Wannier orbitals and minimal-basis tight-binding Hamiltonians for twisted bilayer graphene: First-principles approach. *Physical Review Research* **1**, 033072 (2019).

38. Nuckolls, K. P. *et al.* Strongly Correlated Chern Insulators in Magic-Angle Twisted Bilayer Graphene. *arXiv:2007.03810 [cond-mat]* (2020). 2007.03810.

Acknowledgments: We acknowledge discussions with Andrea Young, Gil Refael and Soudabeh Mashhadi. The device nanofabrication was performed at the Kavli Nanoscience Institute (KNI) at Caltech. **Funding:** This work was supported by NSF through grants DMR-2005129 and DMR-1723367 and by the Army Research Office under Grant Award W911NF-17-1-0323. Part of the initial STM characterization has been supported by CAREER DMR-1753306. Nanofabrication performed by Y.Z. has been supported by DOE-QIS program (DE-SC0019166). J.A. and S.N.-P. also acknowledge the support of IQIM (an NSF Physics Frontiers Center with support of the Gordon and Betty Moore Foundation through Grant GBMF1250). Y.P. acknowledges support from the startup fund from California State University, Northridge. A.T., C.L., and J.A. are grateful for support from the Walter Burke Institute for Theoretical Physics at Caltech and the Gordon and Betty Moore Foundation's EPiQS Initiative, Grant GBMF8682. Y.C. and H.K. acknowledge support from the Kwanjeong fellowship.

Author Contribution: Y.C. and H.K. fabricated samples with the help of with the help of R.P., Y.Z., and H.A., and performed STM measurements. Y.C., H.K., and S.N.-P. analyzed the data. Y.P. and A.T. implemented models. Y.P., A.T., C.L., provided theoretical analysis supervised by J.A. K.W. and T.T. provided materials (hBN). S.N-P. supervised the project. Y.C., H.K, Y.P., A.T., C.L., J.A. and S.N-P. wrote the manuscript.

Figure legends:

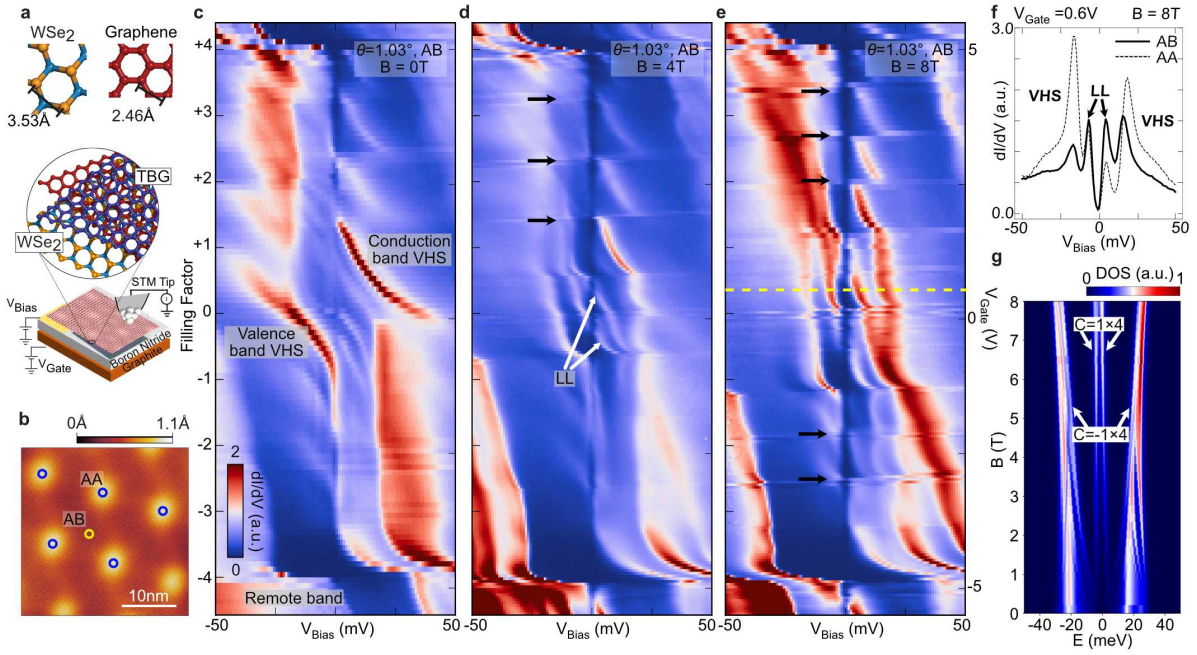

Figure 1 | Spectroscopy of MATBG with magnetic field at 2 K. a, Schematic experimental setup. MATBG is placed on a monolayer WSe_2 and supported by hBN. A graphite gate resides underneath. Inset shows details of WSe_2 and graphene crystal structure. **b**, Typical topography showing a moiré pattern at the magic angle ($V_{Bias} = -400$ mV, $I = 20$ pA). **c-e**, Point spectra on an AB site at $\theta = 1.03°$ as a function of V_{Gate} for magnetic fields $B = 0$ T (**c**), $B = 4$ T (**d**), and $B = 8$ T (**e**) applied perpendicular to the sample. Panel (**c**) shows the evolution of the zero-field density-of-states peaks originating from flat-band VHS. As each of the peaks crosses the Fermi energy, a cascade of transitions appears, manifested here as splitting of the VHS into multiple branches close to integer filling factors ν. Features observed near the CNP are discussed further in Methods, section 7a. Finite-field measurements in (**d, e**) reveal Landau levels forming around charge neutrality (ν = 0), along with newly formed field-induced gaps (black arrows) visible as a suppression of dI/dV conductance. **f**, Conductance linecuts at $V_{Gate} = 0.6$ V and $B = 8$ T on AA and AB sites. Landau levels are more visible on the AB site due to reduced VHS weight. Since the large intensity of VHS peaks on the AA sites can obscure some of the fine features related to high fields, we focus on the AB sites throughout the paper (see Extended Data Fig. 2 for AA-site spectra). **g**, Energy spectrum calculated from the ten band model with parameters chosen such that the relative peak positions match the experimental data in (**f**). Most LLs merge into the electron and hole VHS that each carry Chern number $C = -1$, while two isolated LLs at charge neutrality remain around zero energy and both carry $C = +1$. Due to spin-valley degeneracy the total Chern number for zLLs and VHS is then $C = +4$ and $C = -4$.

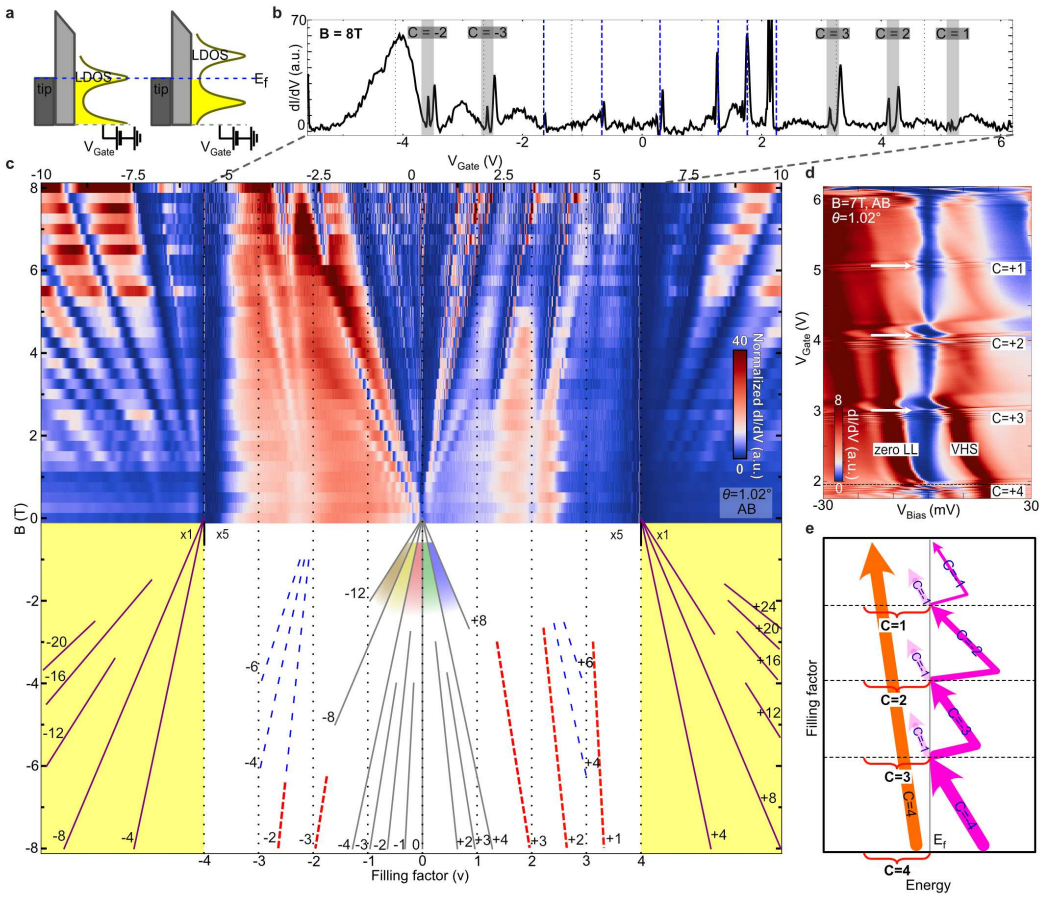

Figure 2 | Local Density of States (LDOS) Landau fan and gaps induced by Chern insulating phases. **a**, Principle of acquiring LDOS Landau fan. Conductance $dI/dV \propto$ LDOS is measured while sweeping V_{Gate} to change carrier density at fixed $V_{Bias} = 0$ mV. **b**, Example linecut taken at B = 8 T and -6 V < V_{Gate} < 6 V. Insulating phases appear as LDOS dips. Chern insulating phases and LLs are indicated by grey regions and blue vertical lines, respectively. The position of these lines is obtained from the slopes in (**c**). **c**, LDOS Landau Fan diagram at an AB site for θ = 1.02°. LDOS data, taken by sweeping V_{Gate}, is normalized by an average LDOS value for each magnetic field (separately for flat and remote bands). Black solid (blue dashed) lines indicate gaps between LLs originating from the CNP (half-filling). Purple lines on the yellow background show the LL gaps in remote (dispersive) bands. Magnetic-field-activated correlated Chern insulator gaps are marked by red dashed lines. The signal in the flat-band region is multiplied by five to enhance visibility in relation to the remote bands. The uncertainty in V_{Gate} of the filling factor $\nu = \pm 4$ position is approximately 0.1 V, see Methods, section 4. The color coding of regions near CNP separated by LL gaps mark different Landau levels in Fig. 4. **d**, Point spectra on the same AB point as in (**c**) as a function of V_{Gate} taken at B = 7 T, highlighting the crossing of the electron-side VHS in magnetic field. Chern insulator gaps corresponding to $C = 3$, $C = 2$ and $C = 1$ are indicated by white arrows. The gaps are accompanied by resonances (horizontal features) originating from quantum dots formed within the insulating bulk (see Methods, section 5). Similar features are also observed on the hole side (see Extended Data Fig. 5). **e**, Schematic of the cascade in magnetic field. Each time the VHS crosses the Fermi energy, a Chern gap appears and the corresponding band Chern number changes.

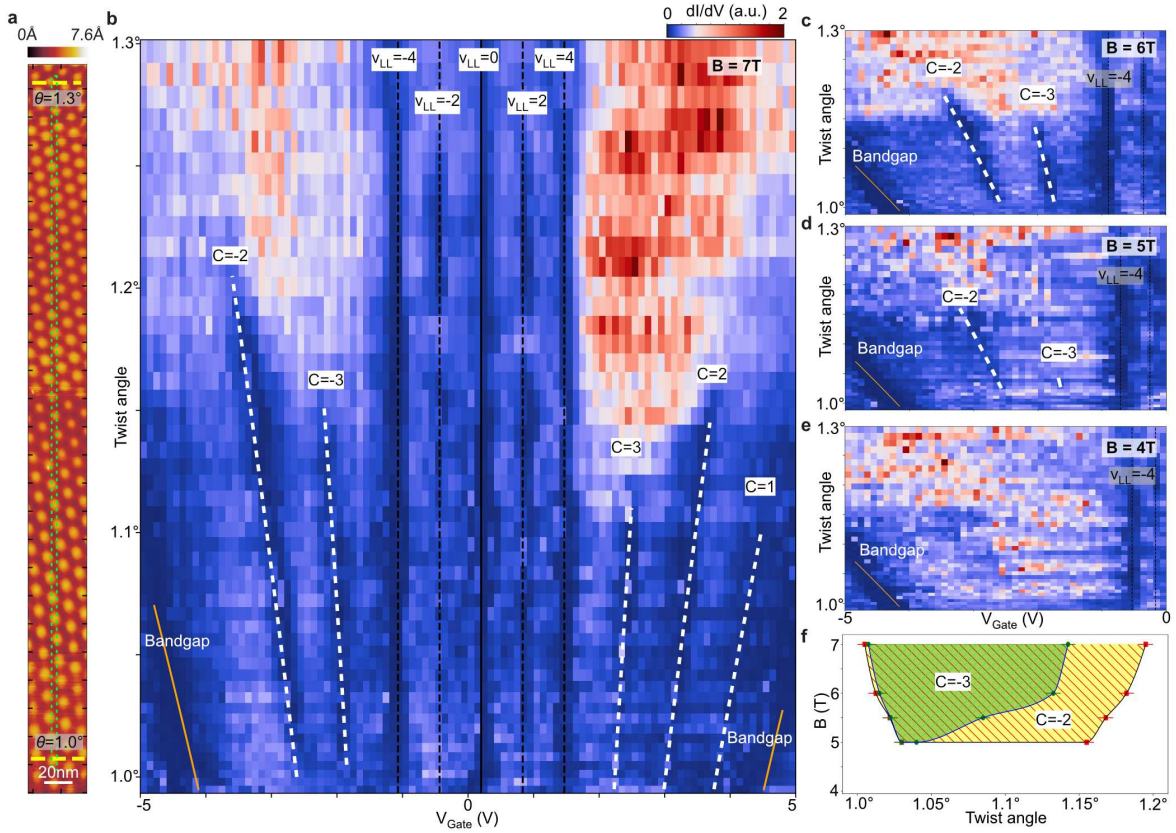

Figure 3 | Angle and magnetic-field dependence of the LDOS and identification of Chern insulators. a, Topography of a 40nm x 520nm area where twist angle gradually changes from $1.3°$ (top yellow line) to $1.0°$ (bottom yellow line); tunneling conditions are $\mathrm{V_{Bias}} = 100$ mV, $\mathrm{I} = 20$ pA. **b**, Conductance at $\mathrm{V_{Bias}} = 0$ mV and $\mathrm{B} = 7$ T taken at different spatial points—characterized by different local twist angles θ—and for different $\mathrm{V_{Gate}}$. Measurements were spatially averaged over the horizontal direction within the green dashed box shown in (**a**). Chern insulating gaps develop only in a certain range of angles near the magic angle. The $\mathrm{V_{Gate}}$ positions of the Chern insulating phases emanating from the integer fillings shift with local twist angle θ since the non-zero filling depends on the moiré unit cell area $\mathrm{A_m} = \sqrt{3}L_m^2/2$. Landau level gaps originating from the CNP, by contrast, do not shift with $\mathrm{V_{Gate}}$. **c-e**, Magnetic-field dependence of the LDOS for hole doping (-5 V $< \mathrm{V_{Gate}} <$ 0 V) at $\mathrm{B} = 6$ T (**c**), $\mathrm{B} = 5$ T (**d**), and $\mathrm{B} = 4$ T (**e**). The Chern insulating gaps disappear as the magnetic field is lowered. **f**, Reconstructed phase diagram showing the range of fields and angles where $C = -2$ and $C = -3$ Chern insulators are observed. In the shaded regions the suppression of LDOS due to Chern insulators is prominent. See Extended Data Fig. 6 for high-resolution data resolving the $C = -1$ state.

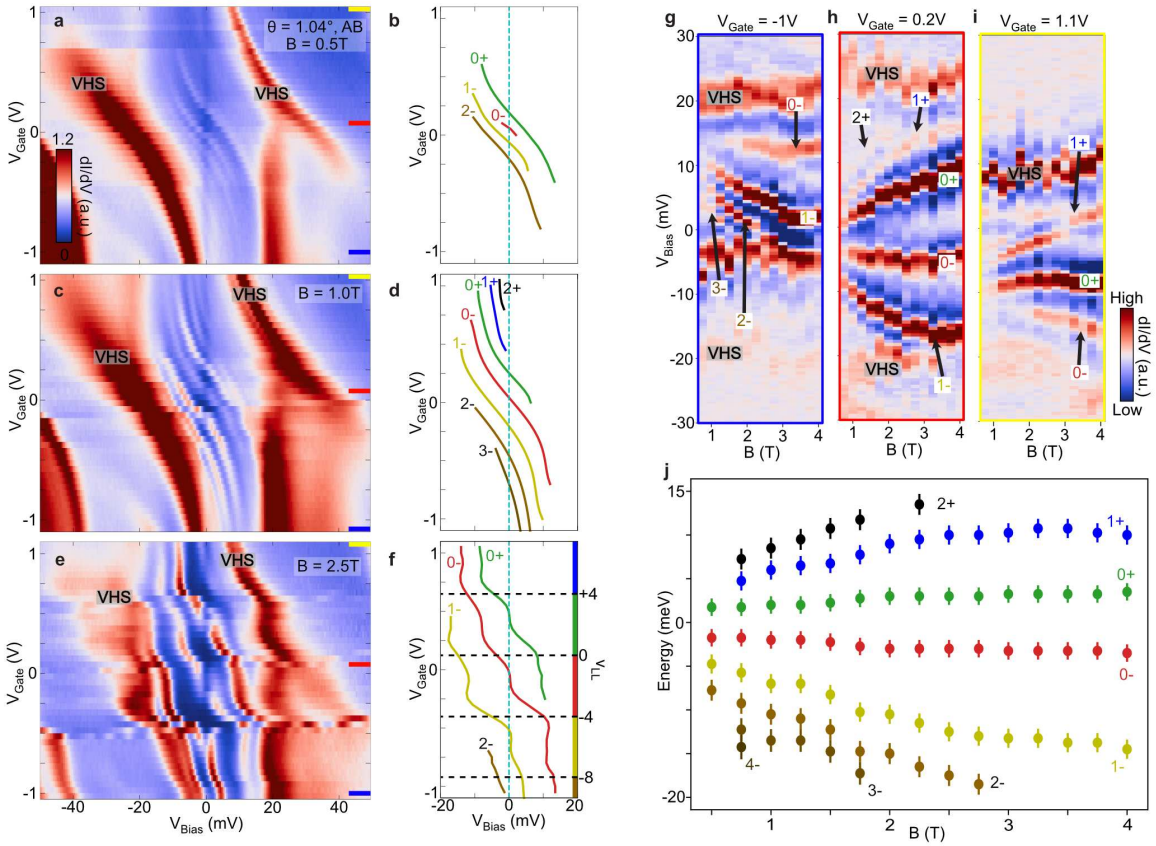

Figure 4 | **Evolution of Landau levels from charge neutrality**. **a-f**, Point spectra as a function of $\mathrm{V_{Gate}}$ (**a,c,e**) and schematics tracking the evolution of Landau levels (**b,d,f**) for $\mathrm{B} = 0.5\mathrm{T}$ (**a,b**), $\mathrm{B} = 1\mathrm{T}$ (**c,d**), and $\mathrm{B} = 2.5\mathrm{T}$ (**e,f**). At the Fermi energy, each Landau level is equally separated in electron density ($\mathrm{V_{Gate}}$) as marked by the Landau-level filling ν_{LL}, indicating four-fold degeneracy of each level. **g-i**, Linecuts at $\mathrm{V_{Gate}} = -1$ V (**g**), $\mathrm{V_{Gate}} = 0.2$ V (**h**), and $\mathrm{V_{Gate}} = 1.1$ V (**i**) illustrating the LL spectrum change with magnetic field. A smooth background was subtracted to enhance visibility. The indicated LLs were identified in (**b,d,f**). **j**, Combined energy spectrum for LLs around charge neutrality. Zero energy is set as the midpoint between $0+$ and $0-$ levels. Error bars in **j** are set by the measured width of the corresponding LLs.

Methods

1 Device fabrication

The device in this study was fabricated with the Polydimethylsiloxane (PDMS)-assisted stack-and-flip technique developed in our previous work[20]. Thick ($\sim$30nm) hBN, monolayer WSe_2 (purchased from HQ Graphene), and monolayer graphene are exfoliated on SiO_2 and identified optically. We used a poly(bisphenol A carbonate) (PC)/PDMS stamp to pick up hBN, WSe_2, and used the stack to tear and twist graphene layers[17], all at $\sim 90^{\circ} C$. We manually rotated the two graphene pieces by $\approx 1.0^{\circ}$. The entire stack attached to PC is then transferred onto a clean PDMS, twisted bilayer graphene (TBG) side facing the PDMS. We dissolve PC in N-Methyl-2-pyrrolidone (NMP) and the stack is transferred on a chip with a graphite gate and gold electrodes. In the final step, TBG is connected to the electrodes by another graphite flake. This method results in good sample quality where we can easily find a contamination-free area of dimensions more than 400nm $\times$ 400nm (Extended Data Fig. 1b) and negligible surface corrugation due to graphite back gate.

2 STM measurements

The STM measurements were performed in a Unisoku USM 1300J STM/AFM system using STM mode. We used a platinum iridium (Pt/Ir) tip, first prepared on a Ag(111) crystal. The tip quality is verified by measuring quasiparticle interference and a spectrum that shows the Ag(111) surface state. Additionally, the tip has been cleaned on the MATBG sample by pulsing on the gold electrode and verifying the resulting spectrum[39]. It is likely that the final tip also contains Au atoms. All the features reported here are robust with more than ten different microtips. The measurements were performed at 2K and the lock-in parameters were modulated at voltage $\mathrm{V_{mod}} = 0.5 - 1$ mV and frequency $f = 973$ Hz; set parameters for dI/dV were $\mathrm{V_{Bias}} = 100$ mV and $\mathrm{I} = 1$ nA, unless specified otherwise. The piezo scanner was calibrated on a Pb(110) crystal. The twist angle uncertainty in MATBG measurements is $\pm 0.01^{\circ}$, originating from measured lengths in topography.

The LDOS-Landau fan measurements shown in Fig. 2c were performed by taking STM data in the feedback off mode while sweeping $\mathrm{V_{Gate}}$. After the data set is collected, we change the magnetic field while keeping track of the same spatial position and turning the feedback on. For each magnetic field the LDOS data at the Fermi energy is normalized by the average value.

3 Effects of WSe_2

One of the main differences between this work and previous MATBG results is the use of monolayer WSe_2 as a substrate. This approach enables finding larger areas (400 nm$\times 400$ nm) that are cleaner and have much less twist angle disorder. Apart from this technical difference, the effects

of spin-orbit interaction (SOI), studied in Ref. 17, have corresponding energy scales of 1 meV—similar to the Landau level broadening observed with STM at 2K. For this reason, we believe that SOI effects do not play a critical role in the results reported here. Also the features observed in zero field qualitatively match results obtained in MATBG on hBN[8]. However, it is plausible that some WSe_2 related effects[40] combined with different measurement geometry, such as possible enhancement of Rashba SOI, may affect details of the MATBG band structure. Future studies will be focused on a systematic investigation of MATBG placed on different substrates.

Based on optical inspection (Extended Data Fig. 1a), WSe_2 and MATBG are not aligned. Also, since WSe_2 and graphene have very different lattice constants, in contrast to hBN, global C_2 symmetry breaking is unlikely even in the case of perfect alignment. Importantly, our STM measurements do not show any C_2 symmetry-breaking signatures in electronic structure, and we find that signatures in topography of the possible moiré pattern between MATBG and WSe_2 are much weaker compared to similar signatures that can be observed in MATBG/hBN structures. This is not surprising, as the MATBG/WSe_2 moiré-pattern length scale is expected to be around 1 nm and thus comparable to inter-atomic distances.

4 Filling-factor assignment

From the LDOS Landau fan diagram (Fig. 2c), we can precisely identify gate voltages that correspond to origins of different LLs and Chern insulator states. Once gate voltages corresponding to ν=0 and ν=$\pm$4 (sometimes also $\pm$2) are identified, conversion between gate voltage and filling factor is fully defined. We have verified that this conversion also gives twist angles that match the values estimated from topography. This approach, equivalent to the one previously used in transport measurements, is much more precise than the alternative methods used in all previous MATBG STM measurements[8,19,20,22,38], where LDOS fan diagram is missing and the filling factor assignments are more ambiguous, see Extended Data Fig. 10. By using LDOS Landau fan, the full filling position can be determined with the error less than about 0.1 V or equivalently the error in filling factor is 0.07 electrons/moiré unit cell. This is a factor of 3-5 smaller error in comparison to determining filling factor from the half-filling positions at zero magnetic field[20].

5 Quantum-dot formation

In our high resolution spectra, various gaps at the Fermi energy are accompanied by nearly horizontal resonance peaks and Coulomb diamonds. For example, band gaps between the remote bands and the flat band (Extended Data Fig. 4a at $V_{Gate} \sim \pm 6$ V), gaps between LLs (Fig. 4e and Extended Data Fig. 4b), and the Chern insulating gaps (Fig. 2d) all show resonances around the gaps. We note that the majority of resonances and Coulomb diamonds are formed *below* (in V_{Gate}) the expected gap position from the LDOS Landau fan. This observation can be explained by quantum-dot formation around the tip. Since the STM tip and graphene have different work

functions[20], even at zero bias the tip acts as a top gate and slightly dopes the region in the immediate vicinity. The likely presence of Au atoms on the tip and observed positions of resonance peaks are both consistent with tip-induced hole-doping underneath. Consequently, as we increase $\mathrm{V_{Gate}}$ the global sample enters the insulating regime first, and the area underneath the tip can still be conducting—thereby creating a conducting island (i.e., quantum dot) and consequent resonances. Further doping will bring the area underneath the tip to the gapped phase, explaining resonances being below the gap in $\mathrm{V_{Gate}}$. We interpret the resonances and observed Coulomb diamonds as direct evidence of fully developed gaps, since quantum dots only form when the insulating-phase resistance exceeds the resistance quantum. Due the presence of quantum dots, extracting exact values of Chern insulating gaps is not straightforward, as both the Chern gaps and the quantum dot charging energy (typically $2-3$ meV) are comparable.

6 Magnetic-field dependence of the cascade of phase transitions

Extended Data Fig. 3 shows point spectra at magnetic fields from $\mathrm{B}=4$ T to 8 T. Positions of the dashed lines are calculated from the slopes in the LDOS Landau fan diagram with the appropriate Chern numbers. As discussed in the main text, for the conduction band, the onsets of the cascade of transitions, where the LDOS is pushed up away from the Fermi energy, match well with the positions expected from the Chern number and magnetic field. For the valence band, onsets of the cascade do not change until $\mathrm{B}=6$ T, where the correlated Chern insulating phases start to occur. For $\mathrm{B}>6$ T, the cascade onsets also match with the Chern number lines. We note that with or without a magnetic field, cascade features are more visible in the conduction band, as the LDOS at the Fermi energy becomes very low after crossing each cascade transition. In the valence band, however, LDOS at the Fermi energy is not sufficiently suppressed after the transition. For example, around $\nu\sim-1$ the VHS peak is still pinned to $\mathrm{E_F}$ while a small amount of spectral weight is pushed away; in contrast, at $\nu\sim1$ the whole VHS peak is lifted from $\mathrm{E_F}$. This observation again illustrates the electron-hole asymmetry present in MATBG and is consistent with our observation in the LDOS Landau fan (Fig. 2c) that Landau levels originating from the CNP may still be visible beyond $\nu=-1$ filling.

7 Magnetic-field dependence of flat-band Landau levels

a. Landau Levels and zero-field features near the CNP: As shown in Fig. 4, in our experiment we can resolve Landau levels around CNP down to $\mathrm{B}=0.5$ T (measured at $\mathrm{T}=2$ K). This resolution is in line with transport measurements taken at similar temperatures. However, even at zero magnetic field, we often see small additional LDOS peaks around the CNP within the VHS (see Fig. 1c); note that their intensity is much lower compared to the main LDOS peaks (VHS) that are determined by the flat parts of the band structure. Mostly likely, these minor peak features at $\mathrm{B}=0$ T are related to MATBG band structure details that are not captured by simple continuum models. Recent *ab-initio* modeling suggested that the γ points in the moiré Brillouine zone can be significantly distorted, with local minima/maxima residing close to the Dirac points[31]. These

local extrema in the band structure would manifest as small peaks in the LDOS observed by STM. We also note that similar fine LDOS peaks at $\mathrm{B} = 0$ T were recently observed in a very different quantum material with Dirac dispersion[41], possibly indicating that other effects such as local fluctuations in chemical potential can also play a role. Importantly, at fields $\mathrm{B} > 0.5$ T the Landau levels become more prominent and can be easily distinguished from these zero-field features by their systematic shift in magnetic field and $\mathrm{V_{Gate}}$.

b. Quantum Hall ferromagnetism of $0+$ and $0-$ Landau levels: When partially filled, the two four-fold degenerate Landau level closest to the CNP, $0+$ and $0-$, exhibit quantum Hall ferromagnetism at high magnetic fields (Extended Data Fig. 4b,c). Consider the evolution of the $0+$ level. Starting from the top line cut of Extended Data Fig. 4c, as $\mathrm{V_{Gate}}$ is lowered the $0+$ level splits several times when crossing the Fermi energy due to exchange. Each time, only the part of the LDOS corresponding to one of the flavors is transferred above $\mathrm{E_F}$. By tracing the evolution of $0+$, we can resolve splitting between all four flavors. Note, however, that the visibility of such flavor-resolved LLs (i.e., the corresponding LDOS) is not equal, indicating that the filled LLs in the quantum Hall ferromagnetetic states have different spatial distribution. In particular the dI/dV peak at $\mathrm{V_{Bias}} < 0$ mV labeled 2 in the upper part of Extended Data Fig. 4c is of similar height as the one above (labeled 3), whereas the last peak (labeled 1) is quite reduced, i.e., the LDOS there is low. We observe similar LDOS evolution of the $0-$ level. These variations possibly originate from layer polarization. That is, some of the flavor-resolved LL wavefunctions may live predominantly on the bottom layer—thereby reducing the corresponding LDOS measured by the STM tip on the top layer. These effects can also reduce the visibility of different ν_{LL} gaps in Fig. 2 and Fig. 3, where odd ν_{LL} are difficult to resolve ($\nu_{LL} = +1$ is 'missing' in Fig. 2c and $\nu_{LL} = \pm 1, \pm 3$ in Fig. 3; see also Extended Data Fig. 6).

c. Electron-hole asymmetry: Our STM observations highlight electron-hole asymmetry visible in MATBG's Landau level evolution. We note that measurements showing this asymmetry in Fig. 2 and Fig. 3 differ fundamentally from the ones discussed in Fig. 4. Figure 2c and Fig. 3 discuss gaps at the Fermi level that develop due to formation of Landau levels or Chern insulators and access physics close to $\mathrm{E_F}$; in this context, these measurements are similar to transport. The electron-hole asymmetry of MATBG in these measurements is inherited from the gap evolution with magnetic field and $\mathrm{V_{Gate}}$. For example, Fig. 3—which shows the gap evolution with twist angle—suggests that flat portions of the valence flat band that make up the VHS evolve differently from the corresponding conduction band. Concretely, starting from angles above the magic angle, the bandwidth of the valence band narrows more rapidly than the conduction band and becomes sufficiently narrow for the development of Chern insulators at larger twist angles. As the twist angle is further lowered, the bandwidth increases again. By contrast, the bandwidth of the conduction flat band becomes sufficiently narrow to give rise to Chern insulators at lower twists angles (around $1.14°$ at $\mathrm{B} = 7$ T). Ultimately, at around $1°$, our data are consistent with the flat portion of the conduction band becoming narrower than the valence band, given that Chern insulators become visible at lower magnetic fields on the electron side; recall Fig. 2c.

In contrast to this observation of MATBG Fermi-level physics, Fig. 4 discusses the LL energy spectrum when the LLs are far from $\mathrm{E_F}$ and thus reflects directly the asymmetry in the shape of MATBG flat bands near the Dirac points.

8 Theoretical modeling and comparison with experiment

a. MATBG in magnetic field: Chern number assignments In this subsection we discuss the assignment of Chern numbers to the MATBG magnetic field bandstructure shown in Fig. 1g. To understand the Chern number assignment it is helpful to start from monolayer graphene. When placed in a magnetic field[42], graphene's quantum Hall conductivity per spin is quantized in steps of $(2n+1)e^2/h$, where n is a LL index as defined in the main text. By relating this fact with the conventional formula for the quantum anomalous Hall (QAH) conductance per spin, Ce^2/h, we find that the 0th LL has a Chern number of $C = 1$ (note that the sign of C and its relation to the QAH conductance is a convention——we could equally well have specified $C = -1$). With each consecutive LL, the total Chern number of occupied states increases until the VHS when it starts to fall, with the conductance of the two filled bands vanishing[43]. This reasoning holds also for MATBG, where the zLL similarly carries Chern number $C = 1$ [35]. However, as discussed in the main text, because of how flat the original bands are, in high fields it is experimentally difficult to resolve other flat-band LLs beyond the zLL. It is therefore helpful to think of the zLLs individually and group the remaining LLs into two sub-bands centered around the electron/hole VHS. In doing so we can then assign Chern number $C = -1$ to the two "effective" sub-bands containing the VHS, as the overall two bands, when fully filled or empty, must have vanishing Hall conductance (and hence total Chern number zero). In the main text we refer to this VHS centered sub-band as simply VHS.

b. Modeling: We used both continuum and ten-band models to calculate the energy spectrum of MATBG subjected to magnetic fields (see supplementary information for calculation details). The continuum model is known to qualitatively capture the correct physics of twisted bilayer graphene at twist angles away from the magic angle. However, it underestimates the experimentally observed bandwidth energy scale in MATBG by an order of magnitude[20], and thus does not capture the correct low-field LL spectrum near the CNP. This discrepancy is in part expected since strong correlations, alongside atomic reconstruction, play a critical role in the physics of MATBG. For this reason, our analysis also employed the phenomenological ten-band model that keeps track of the MATBG symmetries while also possessing a range of parameters that can be easily tuned to allow for a more direct comparison with the experiment. Results from the continuum model are presented in Extended Data Fig. 7. The ten-band model results, discussed in the context of low-energy LL spectrum, are shown in Extended Data Fig. 9.

9 U/W evolution with magnetic field and the phase diagram of Chern insulating phases

Extended Data Figure 8 shows an estimate of the ratio between the characteristic interaction energy U and kinetic energy W as a function of twist angle θ and magnetic field B. Results from panels a,b follow from a continuum model (see supplementary information for calculation details). The bandwidth W is chosen as the width of the $C = -1$ Chern bands that includes the VHS but not the zero LLs; we respectively denote the bandwidths on the electron and hole sides by W_e and W_h (see Extended Data Fig. 7b). The characteristic interaction scale, as specified in the main text, is taken to be $U = e^2/4\pi\epsilon L_M$. Roughly, beyond a critical U/W we expect cascade transitions to become energetically favorable, leading to the experimentally observed Chern insulator phases. Panels a,b depict constant U/W contours (taking $\epsilon = 5$) for various twist angles, excluding a narrow window close to the magic angle where the bandwidths can not be reliably extracted. These constant U/W contours qualitatively reproduce trends observed in the experiment (Fig. 3f), most notably the minimum of the U/W contours near the magic angle. The model's small but nonzero electron-hole asymmetry—manifest in the shifted contours relative to panels a,b—is also consistent with observations.

The main trends for U/W evolution with magnetic field and twist angle can be captured analytically, thus further elucidating the underlying physics. To proceed, we estimate the dependence of the bandwidth W on magnetic field and twist angle. As shown in Extended Data Fig. 7, each $C = -1$ band narrows with field from its $B = 0$ value W_0 (which is *half* of the full zero-field flat-band bandwidth). We crudely capture this narrowing as follows. First, the inner $C = -1$ band edges, close to the CNP, are modified by LLs descending from charge neutrality with energies $\propto \sqrt{B}$. The outer $C = -1$ band edges in general further squeeze the bandwidth by a model-dependent quantity. For simplicity, however, we take the bandwidth reduction arising from the upper and lower edges of a given $C = -1$ band to be identical. This approximation yields an effective bandwidth

$$W(B) \approx W_0 - 2v_F\sqrt{2eB}\,, \tag{1}$$

where v_F is the twist-angle-dependent velocity of the Dirac cone and the factor of 2 comes from our rough assumption of symmetric band squeezing. The critical field $\mathrm{B_c}$ at which Chern insulators appear, corresponding to the edges of the regions in Fig. 3f, correspond to a solution of $U/W(B_c) = \eta$ (with $\eta > 1$), i.e.,

$$B_c \approx \frac{W_0^2}{8ev_F^2}\left(1 - \frac{1}{\eta}\frac{U}{W_0}\right)^2. \tag{2}$$

We estimate the $\mathrm{B} = 0$ bandwidth as set by $W_0 \sim v_F\kappa$ where $\kappa = 4\pi/(3L_m)$ is the κ point at the corner of the mini Brillioun-zone. Finally, to find a simple expression for v_F as a function of twist angle, we follow Ref. 10 and write

$$\frac{v_F^2}{v_0^2} = \left(\frac{1-3\alpha^2}{1+6\alpha^2}\right)^2 + \delta v_F^2\,, \quad \alpha = \frac{w_1}{v_0\kappa} \tag{3}$$

with $v_0 = 10^6$ m/s the monolayer graphene band velocity and w_1 the moiré interlayer coupling parameter that defines the magic angle. As required[10], at the magic angle the term in parenthesis above vanishes. To allow for a finite bandwidth, we have thus included a broadening parameter δv_F. We plot Eq. (2) for several values of η in Fig. 8c. In the plot we use $\delta v_F = 0.013$, $w_1 = 117$ meV and $\epsilon = 5$. The essential feature of the experimental phase diagram, i.e., the minimum near the magic angle, is correctly reproduced. The observed phase boundary, as reproduced by the numerical estimates of Extended Data Fig. 8a,b, is however much steeper with magnetic field—a feature not captured by the crude approximation for $W(B)$ introduced in Eq. (1). The above analytical and numerical analyses demonstrate the critical role played by the twist angle and magnetic field in forming the Chern insulting states driven by correlations.

10 Landau level spectrum for low fields and MATBG band structure

As discussed in the main text, our LL spectrum, shown in Fig. 4j, provides essential input about MATBG band structure. Besides setting a lower bound on the Dirac velocity through the spacing of LLs, it indicates the likely presence of gapless (or nearly gapless) Dirac cones in the MATBG band structure, contrasting some recent theoretical studies. Here we provide a more detailed analysis of different MATBG band-structure scenarios near the CNP. For this purpose we use the ten-band model and corresponding Hofstadter spectra to qualitatively match the experimental findings. Extended Data Fig. 9a-h provides an overview of the different band-structure scenarios that we considered. Throughout we stipulate that the Dirac points either remain fixed to the κ, κ' points or are gapped, though in practice they may be also shifted by the presence of strain[33]. Such shifts, however, do not have a substantial impact on the energy spectrum of the system or our analysis. In the following, we briefly outline four possibilities for the MATBG band structure:

(i) Dirac cones at κ, κ' are strongly gapped by the presence of strong correlations, and the dispersion around the γ point is inverted as proposed by several recent theoretical studies[32] (Extended Data Fig. 9a,b). This scenario implies that all LLs originate from states near the γ point, which would require an unrealistic linear-like dispersion to accommodate our observed LL structure—most notably, nearly flat zero LLs. It may also imply a fully gapped system around the CNP even at zero field (unless the flat bands touch at the γ point or exhibit some other dramatic reconstruction), which is not consistent with our observations. In our simple simulations, even when the γ point bands do touch, the separation between zero LLs increases much more rapidly than observed in experiments.

(ii) Dirac cones at κ, κ' remain gapless and the flat bands at the γ point merge with the VHS. In this scenario all observed LLs originate from the Dirac dispersion (Extended Data Fig. 9c,d). Energetically this scenario is consistent with the observed spectrum and reproduces all the relevant features including the $\sqrt{B}$ dependence of the LL spacing. However, we stress that in this scenario, likely accidental crossings between LLs originating from different Dirac cones have not been observed. A possible explanation for the absence of these crossings involves Dirac cones be-

ing highly asymmetric, with band curvature leading to different Dirac velocities for electron-like and hole-like excitations. Curvature effects combined with the fact that the energetically shifted Dirac points always reside closer to one of the VHS than the other may explain the absence of certain LLs. That is, the 'missing' LLs could simply be absorbed into the nearest VHS for low fields, before they become visible in experiment ($\sim 0.5 - 0.75$ T).

(iii) Dirac cones at κ, κ' remain gapless, and the dispersion around the γ point becomes heavily inverted—giving rise to a subset of the observed LLs (Extended Data Fig. 9e,f). For example, within this scenario, the Dirac points can contribute the 0+ and 0- levels, while all LLs originate from the γ point inverted band structure. In this explanation the relative separation between 0- and 1- (and between 0+ and 1+) would not be determined by the Dirac velocity, but rather by band-structure details (such as the relative energy difference between Dirac point and inverted γ point bands, as well as shape of the γ centered pocket). Viability of this scenario requires the Dirac velocity v_D to exceed $v_D > 2.5 - 3 \times 10^5$ m/s; otherwise additional Landau levels descending from the Dirac cones would be visible.

(iv) One Dirac cone is gapped and the other merges with a VHS (Extended Data Fig. 9g,h). This scenarios is outlined only for completeness, as it can be easily ruled out based on the main features observed in the Hofstadter spectrum. In general, the crossing between the zero LL and other levels (originating from the other Dirac cone) has to happen at a certain finite field, which was not observed experimentally.

Based on this analysis we believe that only scenarios (ii) and (iii) are plausible for MATBG band structure. Further research is needed to fully distinguish between them. We also note that a small mass term may result in zero LLs that disperse with field. Recall from Fig. 4 that we observed a mild increase in the separation between 0+ and 0- levels as the field increased. This feature is not universal, however, as occasionally these levels would move in parallel or approach each other, consistent with the existence of non-spatially uniform mass term that determined evolution of these levels with field. Future work will be focused on relating the LL evolution to possible strain effects.

Method References:

39. Walkup, D. *et al.* Tuning single-electron charging and interactions between compressible Landau level islands in graphene. *Physical Review B* **101**, 035428 (2020).

40. Wang, T., Bultinck, N. & Zaletel, M. P. Flat band topology of magic angle graphene on a transition metal dichalcogenide. *arXiv:2008.06528 [cond-mat]* (2020). 2008.06528.

41. Yin, J.-X. *et al.* Quantum-limit Chern topological magnetism in TbMn 6 Sn 6. *Nature* **583**, 533–536 (2020).

42. Gusynin, V. P. & Sharapov, S. G. Unconventional Integer Quantum Hall Effect in Graphene. *Physical Review Letters* **95**, 146801 (2005).

43. Hatsugai, Y., Fukui, T. & Aoki, H. Topological aspects of graphene. *The European Physical Journal Special Topics* **148**, 133–141 (2007).

Data availability: The data that support the findings of this study are available from the corresponding authors on reasonable request.

Competing interests: The authors declare no competing interests.

Additional Information

Supplementary Information is available for this paper online.

Correspondence and requests for materials should be addressed to S.N.-P. (s.nadj-perge@caltech.edu).

Reprints and permissions information is available at http://www.nature.com/reprints

Extended Data Figure Legends:

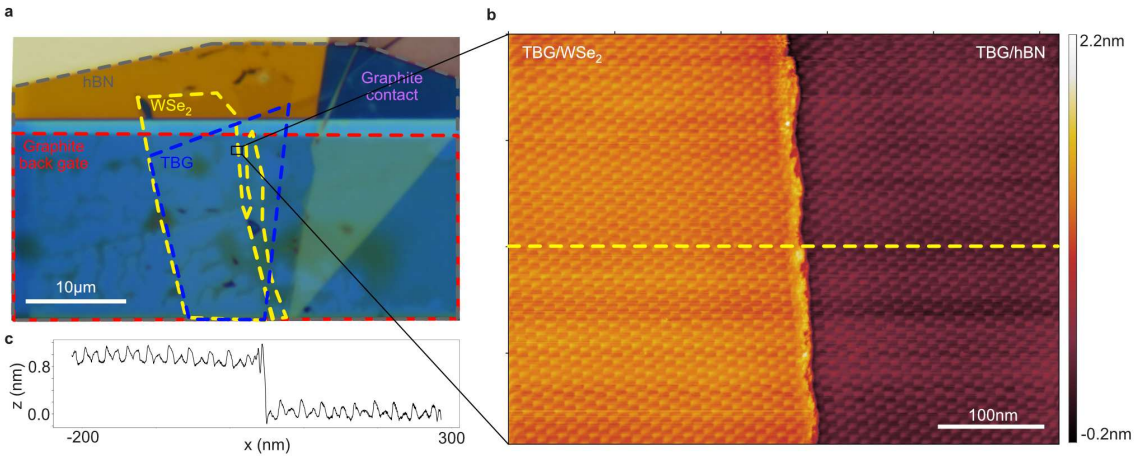

Extended Data Figure 1 | Optical image of the device and STM topography of WSe_2 / hBN boundary. **a**, Optical image of the device. Blue dashed line indicates the region with TBG. **b**, STM topography of a WSe_2 boundary underneath twisted bilayer graphene ($V_{Bias} = -400$ mV, $I = 20$ pA). **c**, Linecut along the yellow dashed line in (**b**). The height difference is around 0.8 nm, which matches with the monolayer WSe_2 thickness. Small ripples originate from the moiré pattern.

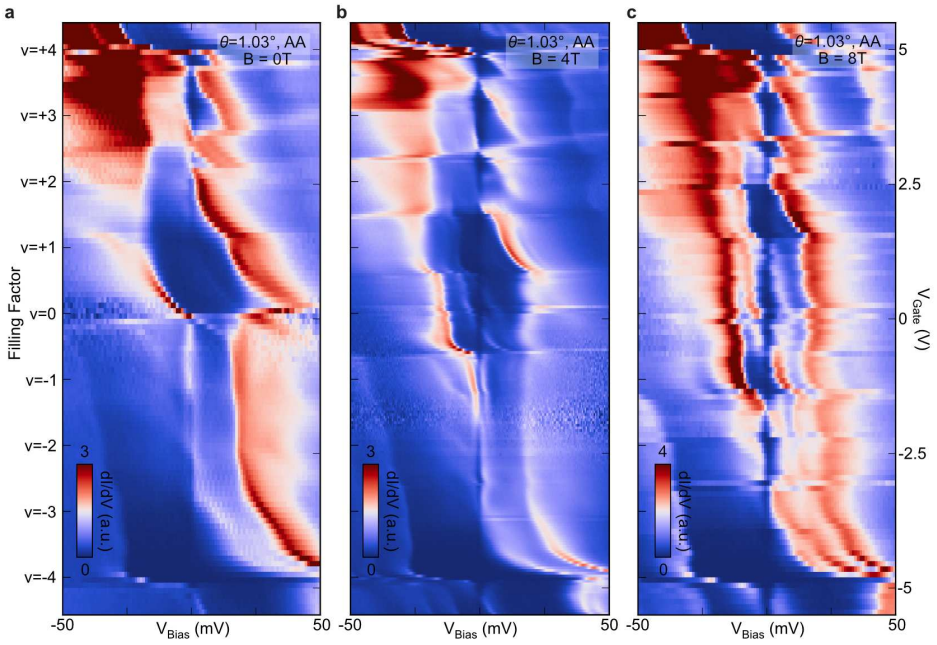

Extended Data Figure 2 | AA site point spectra versus gate voltage with magnetic field. a, $\mathrm{B} = 0$ T. **b**, $\mathrm{B} = 4$ T. **c**, $\mathrm{B} = 8$ T. The area (with $\theta = 1.03°$) is the same as where Fig. 1c-e data are taken. The VHS are more pronounced compared to the AB site, making LL features harder to resolve.

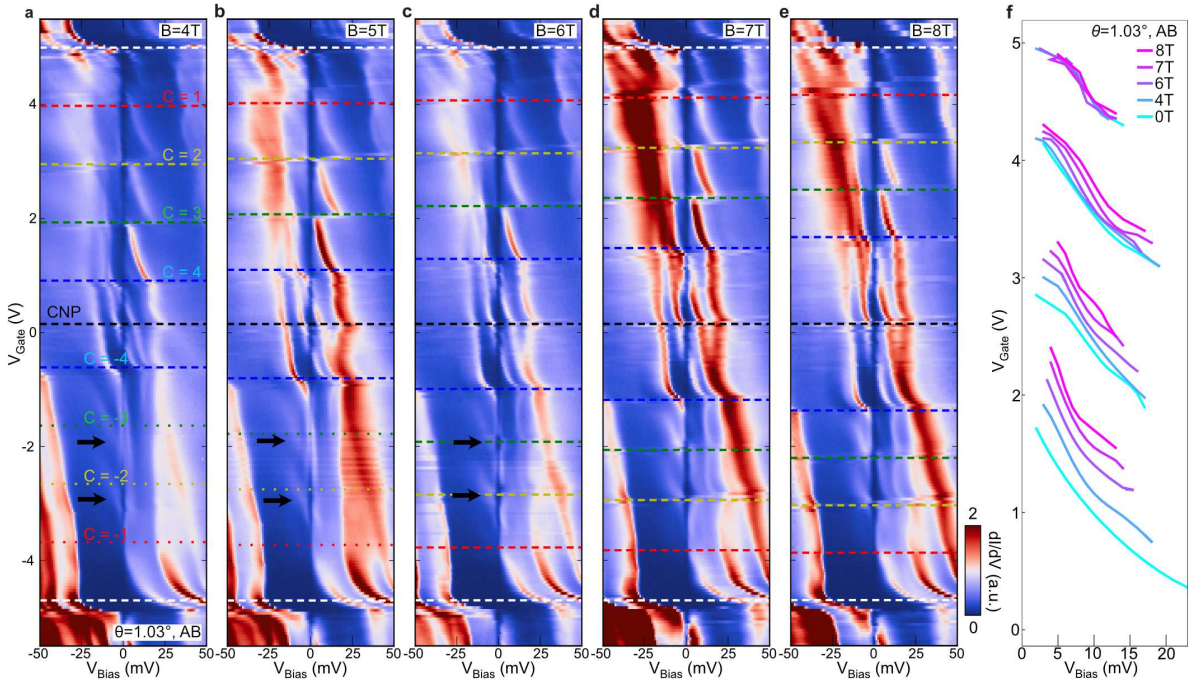

Extended Data Figure 3 | Evolution of cascade with magnetic field. a-e, Point spectra versus gate voltage on an AB site ($\theta = 1.03°$) at B = 4 T (**a**), B = 5 T (**b**), B = 6 T (**c**), B = 7 T (**d**), B = 8 T (**e**). Colored dashed lines indicate positions calculated with corresponding Chern numbers. **f**, Tracking of cascades on the conduction band at different magnetic fields. As the field is increased, the shifting of cascade onsets follows the evolution of Chern insulators. **a** and **e** are the same data as Fig. 1d and e; **b-d** are at intermediate fields on the same area.

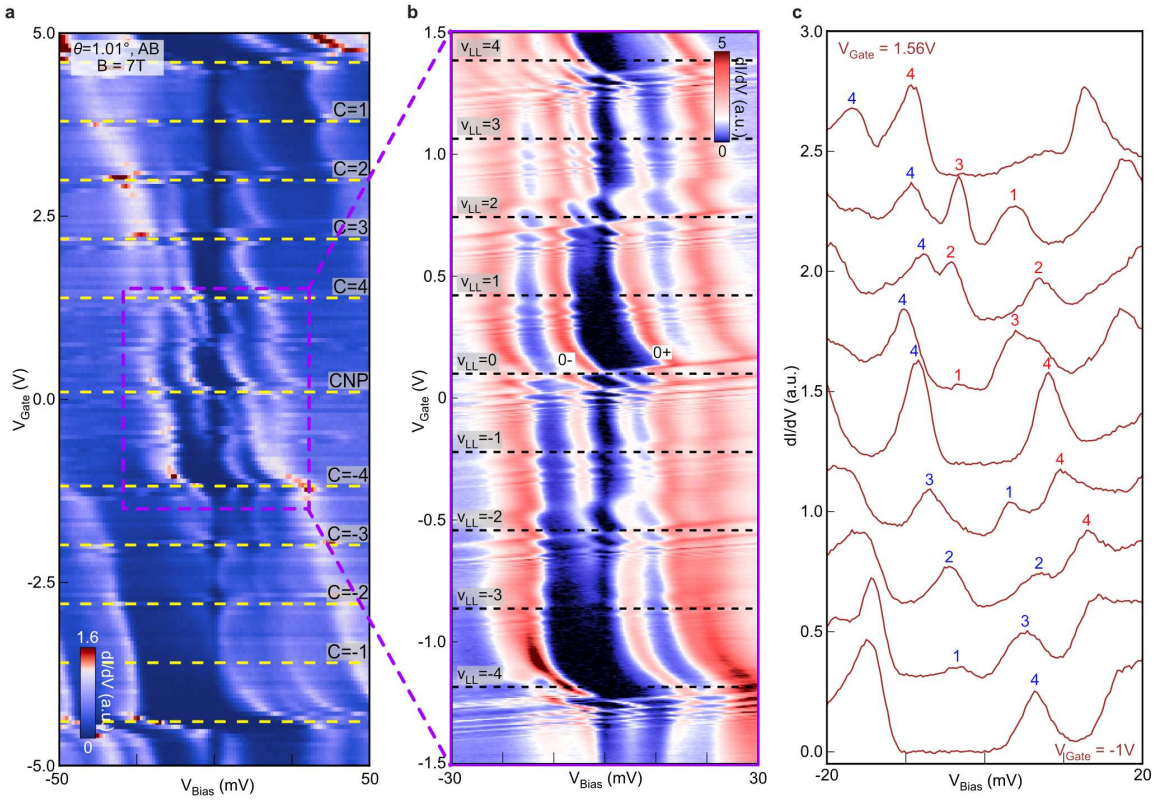

Extended Data Figure 4 | Quantum Hall ferromagnetic states in the zero LL. a, Point spectra on an AB site at $\theta = 1.01°$ as a function of $\mathrm{V_{Gate}}$ for magnetic field $\mathrm{B} = 7$ T. **b**, Zoom-in around the CNP, where zero LLs ($0+$ and $0-$) cross the Fermi energy. The four-fold degeneracy of each zero LL is broken by exchange interactions at the Fermi energy, creating gaps at $\nu_{LL} = -4, -3, \ldots, +4$. **c**, Line cuts when the $0-$ and $0+$ LLs cross the Fermi energy, with vertical offset for clarity. Shifting of the spectral weight of the fourfold degenerate $0-$ and $0+$ LLs cross the Fermi level is clearly visible. Numbers in blue (red) correspond to the number of spin-valley flavors of $0-$ ($0+$) LLs below and above the Fermi level ($\mathrm{V_{Bias}} = 0$) as they cross $\mathrm{E_F}$ near $\nu_{LL} = 4, 3, 2, 1, 0, -1, -2, -3, -4$.

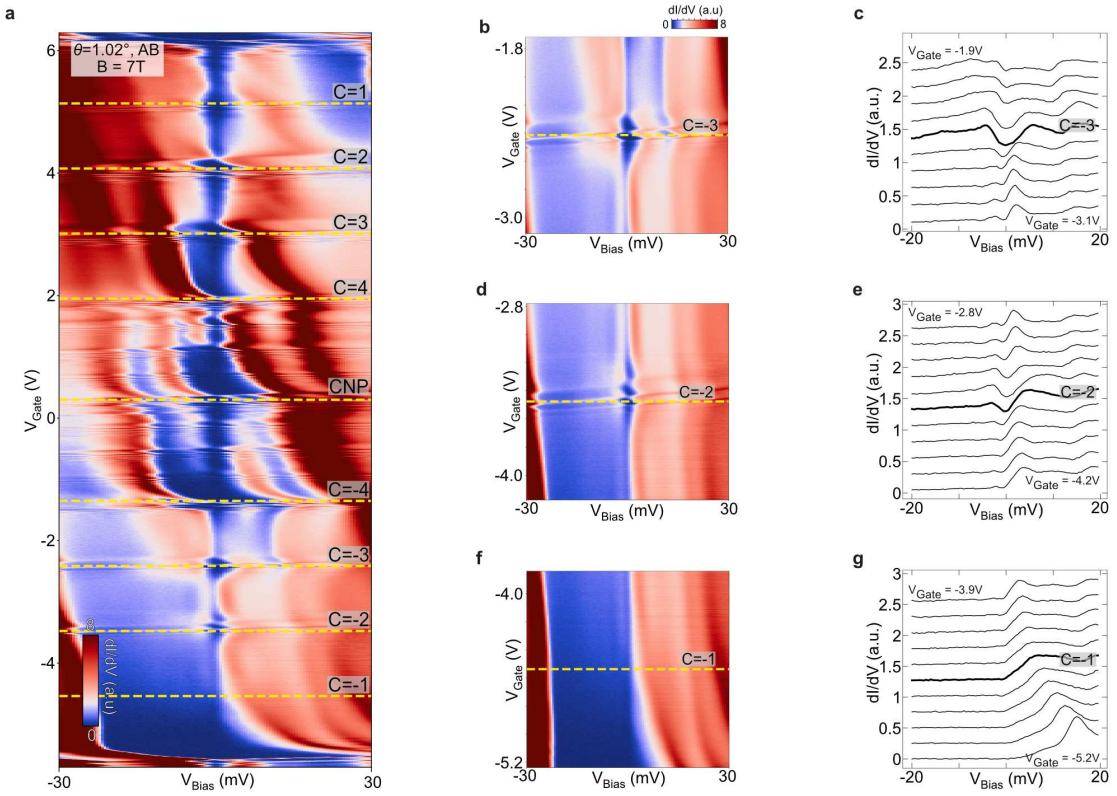

Extended Data Figure 5 | Chern insulating phases in the valence band. **a,** Full gate voltage range of Fig. 2d at $\mathrm{B} = 7$ T, from $\nu = -4$ to $\nu = 4$. **b, d, f,** Zoom-in of Extended Data Fig. 5a around $C = -3$ (**b**), $C = -2$ (**d**), and $C = -1$ (**f**), and their line cuts (**c, e, g**) at various $\mathrm{V_{Gate}}$ with vertical offset. Shifting of the spectral weight across Fermi level is clearly visible in **c** and **e**. The $C = -1$ state was not visible at this angle ($\theta = 1.02°$) and magnetic field ($\mathrm{B} = 7$ T).

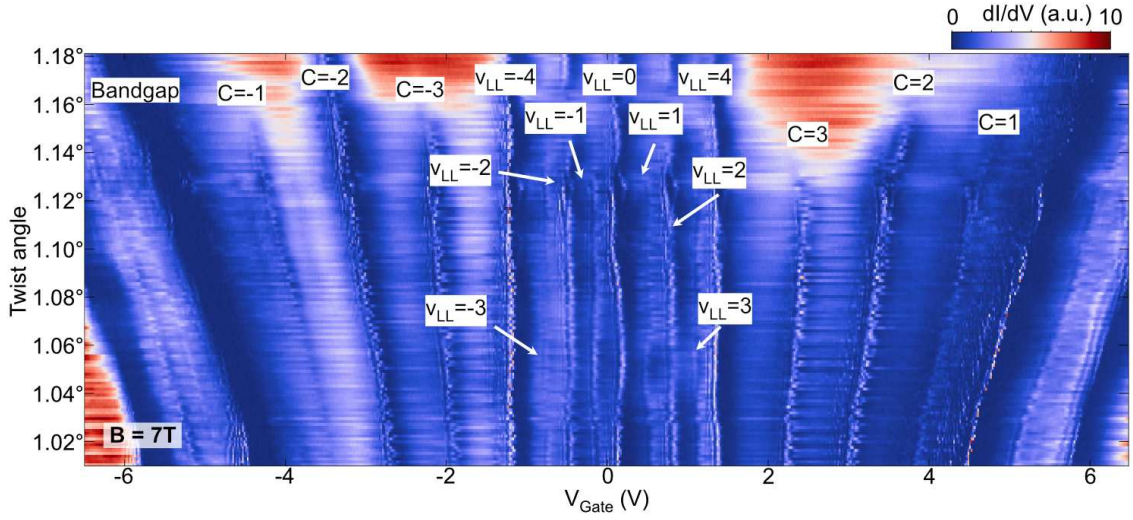

Extended Data Figure 6 | $C = -1$ **phase in high-resolution angle-dependent LDOS map at** $\mathrm{B} = 7$ **T.** Measurements were taken over a 20 nm $\times$ 200 nm area where the twist angle varies continuously from $\theta = 1.01°$ to $1.18°$ by using $\mathrm{V_{Bias}} = 0$ mV and changing the spatial position and carrier density ($\mathrm{V_{Gate}}$). Signature of the $C = -1$ phase as well as $\nu_{LL} = \pm 1, \pm 3$ which were not visible in Fig. 3b, are now observed due to the enhanced $\mathrm{V_{Gate}}$ resolution and the electron-hole asymmetry between Chern phases is even more pronaunced. We note that visibility of $\nu_{LL} = \pm 1, \pm 3$ shows strong spatial dependence while the visibility of $\nu_{LL} = \pm 2, \pm 4$ is high throughout the range.

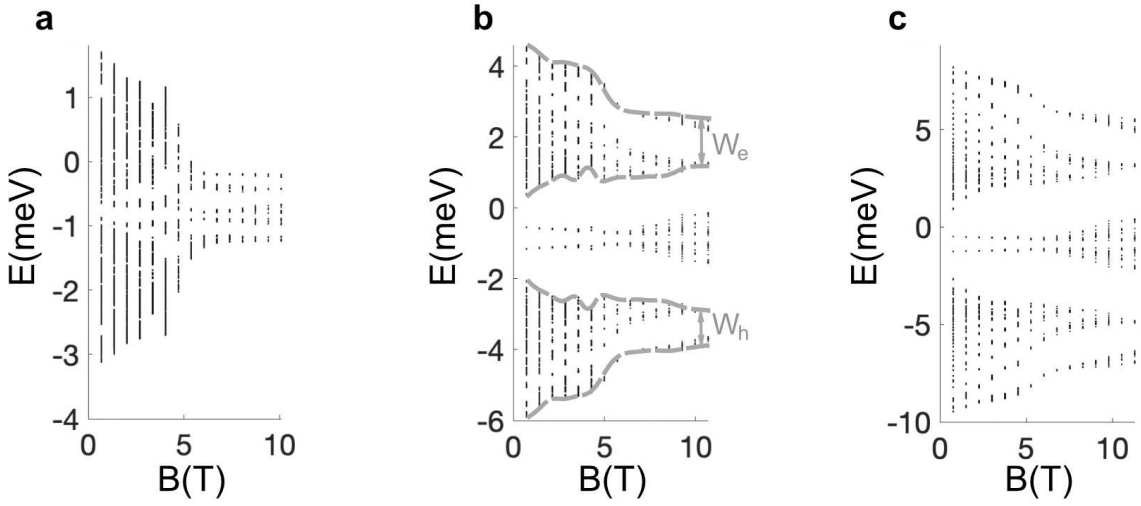

Extended Data Figure 7 | Spectrum of a continuum model taking into account effects of a displacement field. The three panels correspond to twist angles $\theta = 1.03°$ (**a**); $\theta = 1.06°$; (**b**) and $\theta = 1.09°$ (**c**). The displacement field expressed as an energy difference between the two graphene monolayers is 10 meV, and the ratio between AA and AB tunneling amplitudes $w_0/w_1 = 0.4$ is the same for all panels. Similar spectrum is obtained for larger w_0/w_1 ratios. The simple continuum model known to predict correct trends can capture energetically offset Dirac cones by including a displacement field. However, it underestimates the bandwidth of the flat bands (or equivalently the separation between VHS) and exhibits unrealistically strong dependence on the twist angle; even at angles slightly away from the magic angle ($\theta = 1.06 - 1.09°$) the model predicts a $2 - 4$ times smaller bandwidth than observed in the data. All panels feature a well-separated LL starting from each band edge that moves inward with the field. This LL originates from the γ point in the mini Brillouin zone and has not been observed in the experiment. Bandwidth $\mathrm{W_e}$ ($\mathrm{W_h}$) corresponding to conductance (valence) flat VHS sub-band is used for estimating U/W values in Extended Data Fig. 8.

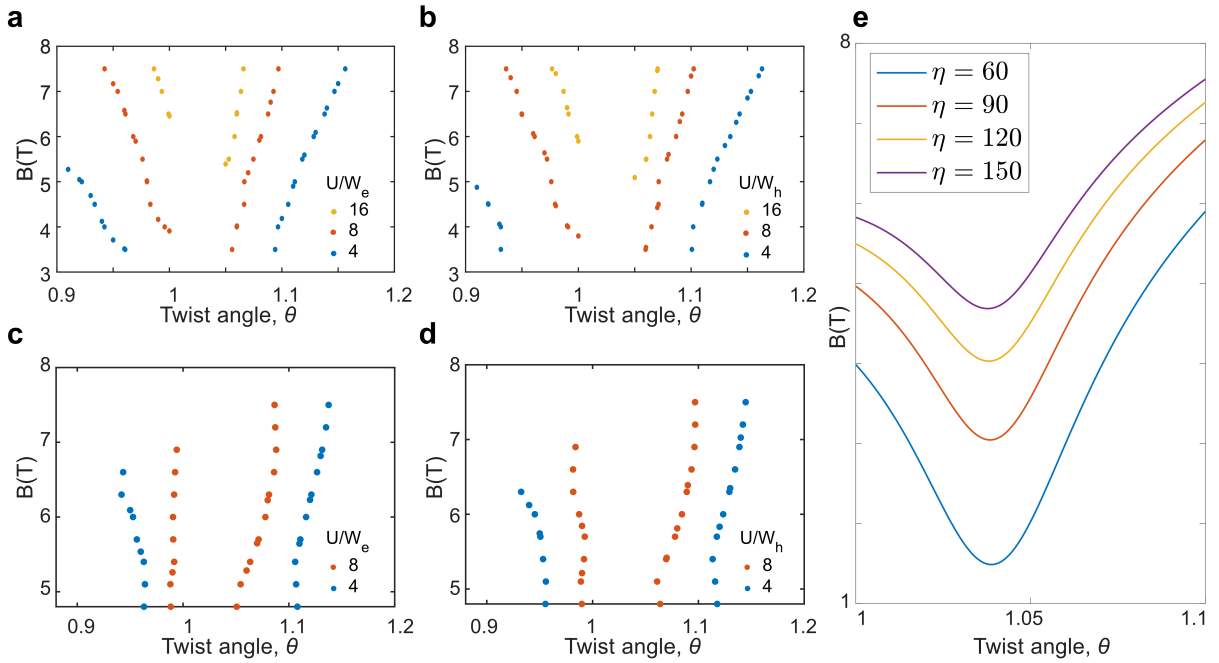

Extended Data Figure 8 | Estimate for the ratio between correlation and kinetic-energy scales $\mathrm{U/W}$ **as function of twist angle and magnetic field**. **a**,**b**, Estimates from the continuum model for the conduction (**a**) and valence (**b**) bands for $w_0/w_1 = 0.4$. **c**,**d**, The same calculation for $w_0/w_1 = 0.7$. **e**, Analytical estimate from Eq. (2). The bandwidth in (**a,b,c,d**) is evaluated as the total width of all levels that together comprise the sub-band that includes VHS (and carry $C = -1$ Chern number). Points very close to the magic angle are not shown due to a lack of clear energy separation from adjacent levels. The plotted constant-U/W curves outline regions where U/W exceeds a threshold value and qualitatively reproduce the structure of the experimental phase diagram where Chern insulating phases are observed (Fig. 3f). In **e**, the large η values are necessary to compensate for the crude approximation of the bandwidth from Eq. (3), which underestimates the bandwidth as compared to the numerical simulation in **a,b,c,d**.

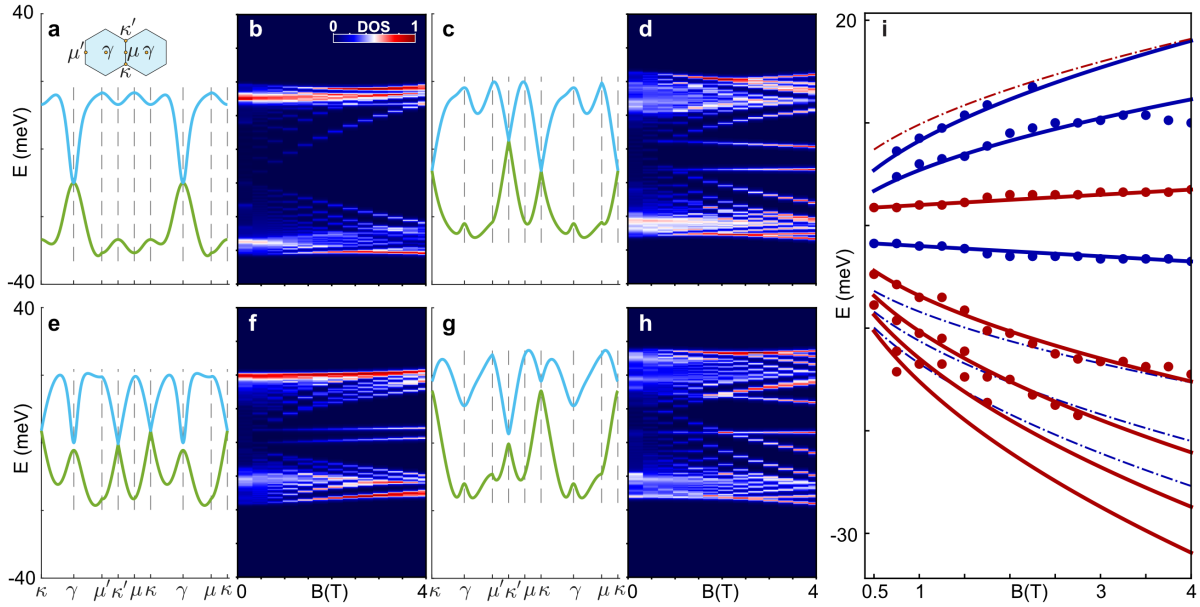

Extended Data Figure 9 | Overview of different possible MATBG band-structure scenarios obtained using the ten band model, alongside the corresponding Landau-level spectra. a, **b**, Scenario (i); **c**, **d**, Scenario (ii); **e**, **f**, Scenario (iii); **g**, **h**, Scenario (iv); The inset in panel **a** shows the relevant high-symmetry momenta. Colors in panels **b**, **d**, **f** and **h** represent the normalized density of states (DOS) obtained via Lorentzian broadening of the Landau spectrum by 0.3 meV. **i**, A possible fit to the data shown in Fig. 4j corresponding to scenario (ii) yielding $v_{D1} = 2.3 \times 10^5$ m/s and $v_{D2} = 1.9 \times 10^5$ m/s for the LLs originating from two two Dirac cones (here marked with red and blue solid lines). The dashed lines correspond to expected LLs that have not been observed, possibly due to relative positions of Dirac cones with respect to VHS. We note that this fitting scenario is not unique. However, all analyzed scenarios give v_D in the range that exceeds 10^5 m/s.

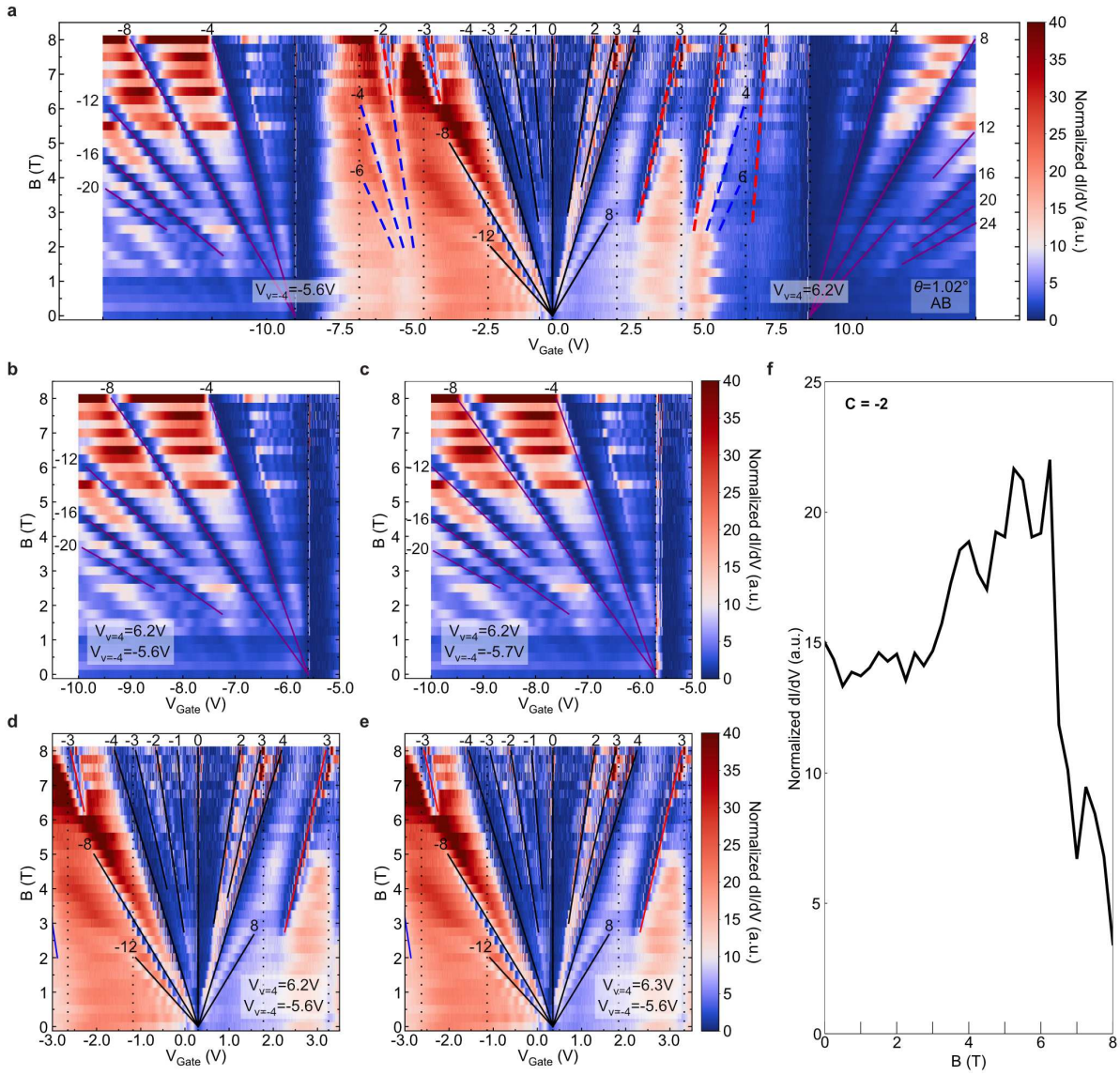

Extended Data Figure 10 | Landau fan diagram overlaid on experimental data for different choices of gate voltages corresponding to $\nu = \pm 4$. a, LDOS Landau fan where the gate voltages $\mathrm{V}_{\nu=-4}$ and $\mathrm{V}_{\nu=4}$, corresponding to $\nu = \pm 4$, are the same as in Fig. 2c. The same gate voltages ($\mathrm{V}_{\nu=-4}$ = -5.6 V and $\mathrm{V}_{\nu=4}$ = 6.2 V) are used in **b** and **d**. **b**, **c**, LDOS Landau fan zoomed-in around hole-side dispersive band with different choice of gate voltages. The choice in **c** ($\mathrm{V}_{\nu=-4}$ = -5.7 V and $\mathrm{V}_{\nu=4}$ = 6.2 V) does not reproduce data well. Similar comparison around CNP where panel **e** corresponds to $\mathrm{V}_{\nu=-4}$ = -5.7 V and $\mathrm{V}_{\nu=4}$ = 6.3V. From this comparison, we extract error in determining $\nu = \pm 4$ to be 0.1 V. All LDOS data are normalized by an average LDOS value for each magnetic field. **f**, Linecut of the LDOS fan Extended Data Fig. 10a along the Landau-level filling of -2 emanating from $\nu = -2$, averaged over a $\mathrm{V}_{\mathrm{Gate}}$ window of 0.04 V. The state above $\mathrm{B} = 6$ T that we identify as a Chern insulating phase is distinguished from half-filling Landau levels by the abrupt drop in LDOS.